



HAL
open science

Towards a 3D-resolved model of Si/Graphite composite electrodes from manufacturing simulations

Chaoyue Liu, Oier Arcelus, Teo Lombardo, Hassan Oularbi, Alejandro A. Franco

► To cite this version:

Chaoyue Liu, Oier Arcelus, Teo Lombardo, Hassan Oularbi, Alejandro A. Franco. Towards a 3D-resolved model of Si/Graphite composite electrodes from manufacturing simulations. *Journal of Power Sources*, 2021, 512, 10.1016/j.jpowsour.2021.230486 . hal-03610979

HAL Id: hal-03610979

<https://u-picardie.hal.science/hal-03610979>

Submitted on 16 Oct 2023

HAL is a multi-disciplinary open access archive for the deposit and dissemination of scientific research documents, whether they are published or not. The documents may come from teaching and research institutions in France or abroad, or from public or private research centers.

L'archive ouverte pluridisciplinaire **HAL**, est destinée au dépôt et à la diffusion de documents scientifiques de niveau recherche, publiés ou non, émanant des établissements d'enseignement et de recherche français ou étrangers, des laboratoires publics ou privés.



Distributed under a Creative Commons Attribution - NonCommercial 4.0 International License

Towards a 3D-resolved model of Si/Graphite composite electrodes from manufacturing simulations.

Chaoyue Liu,^{1,2§} Oier Arcelus,^{1,2§} Teo Lombardo,^{1,2} Hassan Oularbi,^{1,2} and Alejandro A.

Franco^{1,2,3,4*}

¹Laboratoire de Réactivité et Chimie des Solides (LRCS), CNRS UMR 7314, Université de Picardie Jules Verne, Hub de l'Energie, 15 rue Baudelocque, 80039 Amiens Cedex, France

²Réseau sur le Stockage Electrochimique de l'Energie (RS2E), Fédération de Recherche CNRS 3459, Hub de l'Energie, 15 rue Baudelocque, 80039 Amiens Cedex, France

³ALISTORE-European Research Institute, Fédération de Recherche CNRS 3104, Hub de l'Energie, 15 rue Baudelocque, 80039 Amiens Cedex, France

⁴Institut Universitaire de France, 103 Boulevard Saint Michel, 75005 Paris, France

§These authors contributed equally to this work.

*Correspondence: alejandro.franco@u-picardie.fr

Abstract

Composite graphite/silicon (Si) electrodes with low Si weight percentages are considered as a promising anode for next generation Li-ion batteries. In this context, understanding the mesostructural changes due to Si volume expansion and the complex electrochemical interplay between graphite and Si becomes crucial to unlock real-life applications of such composite electrodes. This work presents, for the first time, a three-dimensional (3D) physics-based model for graphite/Si composite electrodes, coupling electrochemistry and mechanics, using as input electrode mesostructures obtained from manufacturing-related Coarse-Grained Molecular Dynamics models. The slurry and dried electrode mesostructure are first generated by considering graphite and additives only, while the Si is included in an additional step. The model herein presented is a step further into obtaining a fundamental understanding of the complex processes happening in graphite/Si composite electrodes, paving the way towards their optimization.

KEYWORDS. Lithium Ion Batteries, Coarse-Grained Molecular Dynamics, Electrode mesostructure, Electrochemistry, Mechanics, Composite electrodes.

Introduction

Lithium ion batteries (LIBs) are already an important part of our everyday life that have enabled the rise of portable electronics. Looking in the short-, middle-term, LIBs also hold tremendous potential to substitute the use of fossil fuels in transportation, with the still incipient Electric Vehicle (EV) market expansion [1–3]. They have also found applications in decentralizing energy storage in residential areas, and they are being adopted for partially solving grid-unbalance issues caused by fluctuations in energy generation of renewable power sources [4,5]. However, increasing the energy density of LIBs remains a primary challenge for enabling some of the aforementioned applications. Focusing on the anode side, graphite is the most used material, thanks to its low price and good cycling stability [6]. Nevertheless, the maximum specific capacity that can be theoretically reached with graphite is 372 mAh/g, which limits the range of use cases for LIBs. In these regards, alloy negative electrodes, and in particular silicon (Si) [7], stands out as a promising candidate for next generation LIB anodes. When fully lithiated, Si forms the $\text{Li}_{15}\text{Si}_4$ alloy, showing a high theoretical specific capacity of 3579 mAh/g, ten times larger than graphite. It also shows an appropriate voltage (~0.4 V) for being adopted as an anode. However, Si undergoes a ~300% volume expansion upon charging, which induces Si particle pulverization, unstable solid electrolyte interphase (SEI) formation and contact loss between Si and conductive additives because of internal stresses [8,9]. All these issues cause major problems for the performance and lifetime of LIBs using Si as anode. Some of these issues, such as the pulverization of the Si particles, can be solved through nanosizing [10], but much of the other problems that hinder the applicability of these anodes remain. Therefore, alternative strategies to incorporate Si in LIB anodes are currently being developed.

Today, much of the focus is now being given to composite electrodes made of graphite and nanosized Si (n-Si) [11,12], where graphite acts as an electrochemically active and mechanically stable framework to buffer the volume expansion of the n-Si particles. Such approach essentially relies on a compromise between cycling stability, provided by graphite, and higher specific capacities, provided by Si. Composite electrodes with low n-Si content (< 25 wt.%) are of particular interest, since they potentially enable manufacturing processes that are compatible with the current LIBs, while significantly increasing their specific capacity, when compared to graphite only electrodes [13]. For instance, as few as 10 wt.% of Si could, theoretically, contribute to approximately half of the electrode's capacity. Still, similar to electrodes made of Si only, the huge volume of expansion of the n-Si particles results in composite electrodes that, to some extent, also suffer from pretty significant mesostructural changes. These changes result in electrode thickness variations [14], loss of electrical particle contact within the mesostructure [15,16], and continued consumption of electrolyte [17], all of which affects the electrode's electrochemical performance [18]. All those phenomena depend on the exact particles location along the electrode, where the heterogeneous distribution of electrode components in 3D becomes important when trying to understand the coupled mechanical and electrochemical behavior of graphite/Si composite electrodes [19,20].

Experimental 3D probing techniques, such as X-ray tomography [19], or the more recently developed scanning spreading resistance microscopy (SSRC) [20], are critical when trying to extract fundamental insights about the mesostructure-performance relationships of battery electrodes in general, and of graphite/Si composite in particular. However, those techniques are too costly to be used systematically, and often require not routinely accessible instrumentations, such as synchrotron beamlines. In addition, those techniques often need to find compromises

between the appropriate resolution/phase contrast needed to resolve certain phases, such as the carbon binder domain (CBD) [21,22], and the sample size, which can hinder mesostructural representativity [20].

In these regards, computational 3D modelling has been proven to be an efficient tool to better understand battery phenomena at the mesoscale [23–29], where relationships between the electrode mesostructure and performance can be elucidated. Concerning the generation of 3D electrode mesostructural models, we can distinguish between two main approaches, each with their own advantages and disadvantages: (i) stochastic generation, where particles are randomly placed or piled on a simulation box until a certain target is met (porosity, particle number, *etc.*) [30,31] and (ii) physics-based simulations, such as Coarse-Grained Molecular Dynamics (CGMD) [25,32,33] and Discrete Element Method (DEM) [25,29,34–36]. A recently developed third option consists of generating realistic 3D electrode mesostructures by generative adversarial networks (GANs) [37,38]. Those models can then be fed to electrochemical models in order to assess their performance as a function of their mesostructural properties [24,27,39].

Returning to our graphite/Si composite electrodes, it should be noted that Si is considered to be a challenging material to model, due to its severe volume change and potential hysteresis upon lithiation/delithiation. Many modelling efforts have been done in establishing the connection between the electrochemical and mechanical behavior of Si [40–45]. Some of these works decouple both phenomena [40,44], while others empirically relate the Si potential to its inner mechanical stress [41–43]. Modeling graphite/Si composite electrodes is even more challenging, and it is currently understudied from a computational perspective. In the work of Sturm *et. al.* [46], the electrode is treated as a single empirical phase, where properties such as open-circuit voltage (OCV) and maximum solid lithium concentration are considered as effective parameters.

Concerning the mechanical behavior of the composite electrodes, most of the studies are done at the experimental level, focusing mainly on macroscopic observables such as the thickness change of the electrode upon lithiation [14,47,48]. As a result, the influence of Si volume expansion on the composite electrode mesostructure still lacks investigation, and this is especially true in modelling, where the 3D location of each electrode component should be resolved explicitly due to the tight link between degradation mechanisms and mesostructure.

This work aims at moving a step forward in the modelling of graphite/Si composite electrodes. Here, we report a new 4D (3D + time) model of a graphite/Si composite electrode, where the graphite and Si electrochemistry and mechanics are coupled. In particular, we show how the electrode mesostructure changes upon galvanostatic discharge as a result of the interplay between Si and graphite. The pristine electrode mesostructure, including graphite, Si particles and CBD is resolved with CGMD, similarly to what has been previously reported by our group [25,32].

2. Methods and models

2.1 Generation of the mesostructural model

The generation of the graphite/Si electrode mesostructures is done in several steps. First, a slurry that only contains graphite and CBD particles is simulated by using the experimental composition of a graphite slurry and the corresponding active material (AM) particle size distribution. However, in this case 10% of the total graphite mass is removed, to be later substituted by Si particles. Then, a drying simulation is performed in order to obtain a tentative dry graphite electrode. In this case, the reference composition for the graphite electrode was 94.8 wt.% of graphite (GHDR 10-4, Imerys), 2.5 wt.% of carbon black (C- NERGY™ super C45), 1.5 wt.% of binder (CMC, ACROS Organics), 1.2 wt.% of additives (1.0 wt.% of SBR, Zeon,

and 0.2 wt.% of TX, Sigma-Aldrich). Here, the graphite particles are considered explicitly, while the additives are considered implicitly in the CBD phase, whose particles intend to represent additive agglomerates. The experimental graphite particle size distribution is shown in Figure S1 in the supplementary information (SI). The graphite particles are approximated as spheres, which is different from the standard flat ellipsoidal graphite, but is nonetheless consistent the experimental shape of the GHDR graphite that we used (Figure S2). Water was used as a solvent and the slurry solid content (SC) was 38%. Differently from our previous model, in which CBD particles accounted for carbon+binder+solvent at the slurry phase and carbon+binder only at the electrode phase [25], here the CBD particles account for carbon+binder only for both slurry and electrode phases, while the solvent is modelled by using devoted particles, whose total volume is calculated to match the experimental SC. On the one hand, the main idea behind the use of particles to model the solvent is to use highly overlapping particles, thus mimicking a continuum medium. On the other hand, the rationale behind using explicit CBD particles in the slurry is the consideration that carbon black particles and binder form aggregates in the slurry, which further densify upon drying, leading to CBD agglomerates at the electrode phase [49–52]. In principle, this would imply using smaller CBD particles (mimicking carbon+binder aggregates) at the slurry phase and mimicking their agglomeration along drying. In this work, for simplicity, and given that the objective of this work is not assessing the dynamics of CBD agglomerate formation, but studying the mesostructure effects of Si expansion in graphite/Si composite electrodes, the CBD particles are kept constant with a diameter of 1.5 μm and a density of 0.866 g/cm^3 . This corresponds to CBD agglomerates with a nanoporosity of ~50%, as measured by previous FIB-SEM measurements [53]. In this type of CGMD simulations, all constituent

particles in the model interact with each other with the Lennard-Jones (LJ) and Granular-Hertzian (GH) force fields (FFs), as introduced by earlier works [25,33].

After the slurry phase is formed, a dry electrode is generated by taking the slurry phase as the input structure and by removing the solvent particles. Then, an additional CGMD simulation is performed in order to equilibrate the dry electrode, by considering ‘harder’ LJ and GH parameters that mimic the formation of a more solid system, as explained in our previous work [25]. Once the graphite dry electrode is formed, the structure is decorated with the remaining 10 wt.% of Si particles and further equilibrated with CGMD simulations. This last step contains two further approximations: the first one concerning the Si particle size and the second one related to the role of n-Si in affecting the slurry phase and the associated drying.

On the one hand, the size of the Si particles we used (300 nm) is larger than the experimental one, since commercial Si nanoparticles range between 40 and 70 nm in diameter. This assumption is justified by the fact that Si nanoparticles hardly ever disperse perfectly in the dry electrode. Instead, they tend to form aggregates [54]. Additionally, this assumption allows us to build a model with a reasonable number of particles, given our computational resources. Figure S3 shows a preliminary calculation of the number of Si particles to be simulated as a function of the targeted simulation box volume and Si particles size, given the aforementioned formulation. As shown, the number of particles quickly rises when considering smaller Si particles, calling for a compromise between mesostructural representativeness and the computational cost (which links to the total number of particles). This compromise is met by selecting a target volume of $30 \times 30 \times 30 \text{ } \mu\text{m}^3$ (even though, the exact final equilibrated volume will depend on the FF parameters) and a Si particle diameter of 300 nm, which results in system that contains ~90000 particles. Even if the Si particles were considered as n-Si aggregates in this work, we must note

that a diameter of 300 nm is still a higher limit for the resistance to fracture upon volume expansion [7].

On the other hand, this model assumes that, due to the relatively low amount of added Si particles (10 wt.%), the slurry structure and associated drying (simulated by using graphite, CBD and solvent particles only) are still representative of the ones obtainable by explicitly considering the Si particles as well, which were added only after the drying step. This late addition of Si allows bypassing the full slurry and drying simulations, which would increase the computational cost by an order of magnitude. Of course, the rheological properties of the slurry without Si nanoparticles must not necessarily have to be similar to the ones of a slurry containing a small addition of Si nanoparticles. In fact, evidence suggests that the rheological properties of graphite/Si slurries differ when using μm -sized and nm-sized Si particles [55]. However, Si in dried electrodes is visible by common microscopy techniques such as Scanning Electron Microscopy (SEM), which allows reproducing its location *ad hoc* without the need of following their particle evolution from the slurry to the dried electrode. This is indeed not the case with CBD particles, thus the need of the full workflow to resolve their position [25]. Still, there are some caveats when building the graphite/Si electrode mesostructures by taking the above considerations into account. Specifically, we note that different aggregation states of Si and conductive carbon particles might also exist for varying composition and SC for the slurry and dry electrodes. Consequently, there could be situations where CBD and Si particles could not be resolved as separated particle beads in the CGMD mode. This would require introducing a new effective particle bead that includes Si + carbon + binder, which would of course have different physical properties when compared to CBD particles alone. However, those physical properties are not well studied yet, which poses a problem when it comes to parametrizing the continuum

model that is later introduced in the text (see Table S2). Therefore, for the purposes of our work, the CBD and Si particle beads are kept separated.

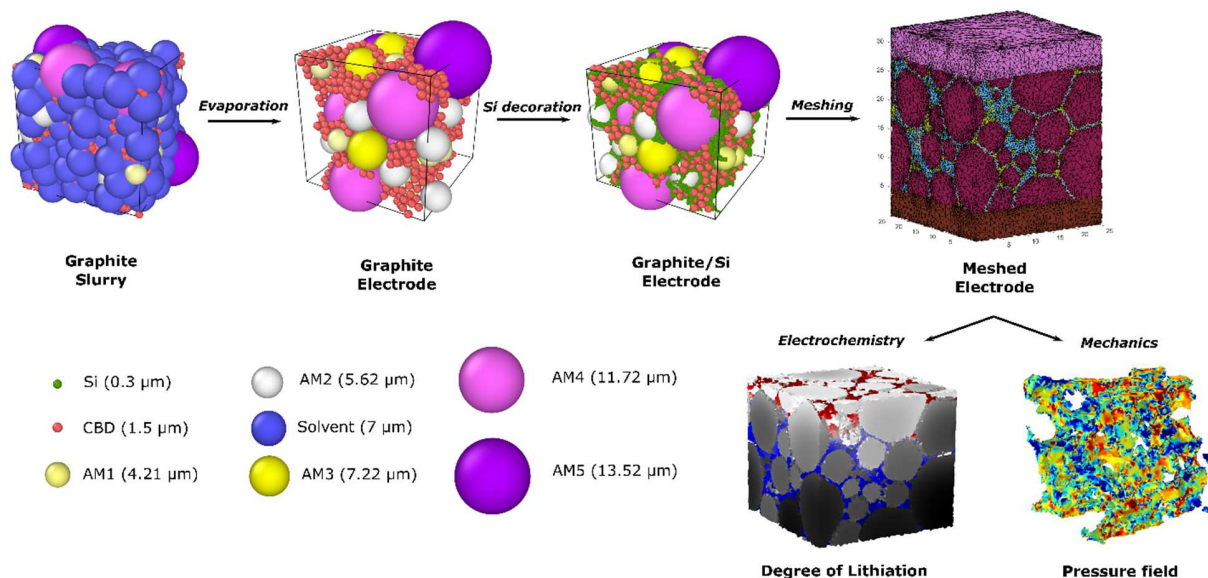


Figure 1: Workflow used in this work. From the simulation of the graphite slurry (top left), to the coupled electrochemical and mechanics simulation (bottom right). The color and size of each particle is shown in the bottom left. The size of the Si particle is exaggerated for improved visibility. The state of charge map is represented in grayscale (red-blue) for graphite (Si) phases, respectively. The stress field represents the stress of the CBD network.

Lastly, we note that the FF parameters for the CGMD model presented in this work are not fully validated to experimental viscosity curves (for the slurry), or porosity and density measurements (for the dry electrode). Instead, here we aim at qualitatively studying the effect of Si volume expansion on a given graphite/Si mesostructure, for which obtaining highly experimentally validated mesostructures is not of paramount importance. Nevertheless, using the above presented method to generate mesostructures has various advantages when compared to cheaper stochastic mesostructure generation. For instance, the model has the potential to be improved by fitting FF parameters to reproduce experimental physical properties. Additionally, DEM methods to simulate electrode calendaring could be easily included in the workflow [25,29].

Summing up, Figure 1 shows the overall workflow used to generate the graphite/Si composite mesostructures. The structures were equilibrated using a Nose-Hoover barostat and thermostat at

300 K and 1 atm. The simulations were performed using LAMMPS molecular dynamics software [56] using periodic boundary conditions in all directions. The FF parameters used for this work are included in Table S1. All simulations were performed in the TGCC Joliot-Curie (CEA) supercomputer, in 64 core AMD Rome (Epyc) processors. More details on the generation of CGMD electrode structures can be found in Ref [57].

2.2 Meshing of the mesostructure

After the graphite/Si mesostructural model is generated, the CGMD structure is first voxelated with an *in house* program and converted to image stacks with voxels sizes of $0.25 \times 0.25 \times 0.25 \mu\text{m}^3$, a little bit smaller than the Si particles. First, it was realized that due to the overlaps between the graphite particles, the meshed structure resulted in a rigid graphite matrix that would not displace the particles as a result of the Si expansion. Therefore, in order to guarantee the free movement of graphite particles, the overlap regions were removed by making sure that at least a $0.5 \mu\text{m}$ gap existed between them, as shown in the meshed electrode in Figure 1. The AM particles were then dilated in order to compensate for the lost volume due to the cutting.

Due to the small size of the Si particles, and in order to avoid the generation of an excessively dense mesh, which would result in prohibitive simulation times, the Si particles were merged together in a homogenized domain. Additionally, in order to guarantee the connectivity of the CBD network, which is not obvious from the particle-like assumption of the CGMD simulations, the CBD phase was further treated with a ‘connect-erode’ process, as illustrated in Figure S4. In short, CBD particles are first connected with a cylinder of the same diameter as the particles themselves and the interface between the CBD and the electrolyte phases is eroded in order to recover the original volume. Lastly, a tetrahedral finite element mesh was generated from the voxelated mesostructures, with the open-source *Iso2mesh* software [58].

2.3 Continuum Model

The mesh was then imported into COMSOL Multiphysics 5.4 to build the 4D-resolved model for the electrochemical and mechanical simulations. The *Lithium-ion Battery, Transport of Dilute Species* and the *Solid Mechanics* modules were used for the electrochemical and mechanical model. All the equations and parameters that are used are listed in Table S2. The CBD phase was considered as a partially open porous material with a 50% porosity, which is also considered in the CGMD simulations. This means that the CBD phase is electronically conducting and permeable to the diffusion of Li⁺ ions. Similarly, due to the fact that Si was meshed as a homogenized domain, the resulting Si domain was approximated as a porous electrode. Within this domain, Si particles were assumed to be close packed, resulting in a domain with a porosity of 26%. Thus, similar to CBD, the Si domain is permeable to Li⁺ ions. Diffusion of lithium within the Si particles was calculated using spherically symmetric Fick's law in an extra dimension. In both CBD and Si phases, the effective diffusion coefficient and electronic conductivity were corrected using the Bruggeman relation. Due to the hysteresis of the Si potential, two open circuit voltage (OCV) profiles must be considered for charge and discharge. In this work, a half-cell model is built, which uses the graphite/Si mesostructural model as the cathode and Li metal as the anode. Then, a single discharge is simulated, which corresponds to the lithiation of the AM. Thus, the corresponding Si OCV curve, as well as the graphite OCV curve were considered separately, as shown in Figure S5.

The outputs from the electrochemical model were then coupled to a mechanical model. In the mechanical model, the electrolyte phase was excluded because it was approximated as a free

deformation domain, assuming that its effect on the deformation of the electrode was negligible. Additionally, since the Si phase is approximated as a porous electrode, the inner stresses that are generated can no longer be directly related to the stresses between the explicit Si particles. Then, the equation of motion takes the form in stationary condition as following, where σ is Cauchy stress tensor:

$$0 = \nabla \cdot \sigma$$

Moreover, graphite, Si and CBD domains are treated as a linear elastic material. Hooke's law is used to describe the relation between the stress and strain tensors:

$$\sigma = C : (\epsilon - \epsilon_{inel})$$

where C is the elasticity tensor, ϵ is the total strain tensor, and ϵ_{inel} is the inelastic strain tensor. Here, ϵ_{inel} contains the information about the swelling of the graphite and Si upon lithium intake. The formula that relates the displacement field u and the strain tensor is written as:

$$\epsilon = \frac{1}{2} [(\nabla u)^T + \nabla u]$$

As already mentioned, both graphite and Si undergo volume expansion with lithium insertion. In fact, even if the volume expansion of graphite (10%) is much smaller than Si (~300%), its contribution to the whole electrode thickness change is non-negligible, since the majority of the AM volume fraction is occupied by graphite [14]. We assumed that the volume of change of both materials follows a linear relationship with the lithium concentration within the particle [59]:

$$\frac{V_m}{V_{0,m}} = x_m \cdot \frac{\Omega_m}{V_{0,m}} + 1$$

where V_m and $V_{0,m}$ are the volume per mole of host material ($m = \text{graphite, Si}$) at the current, and initial states, respectively. x_m is the mole fraction of lithium in the host material, and Ω_m is

the partial molar volume of lithium. The large volume changes of Si also result in large surface area changes, which considerably alter the reaction current densities and the Si overpotential. Therefore, the Si surface area change was taken into account in the electrochemical model through the following formula:

$$A_{Si} = \frac{3}{r_{0,si}} \left(\frac{V_{0,m}}{V_m} \right)^{\frac{1}{3}}$$

where, A_{Si} is the surface area of Si, with units of m^{-1} , and $r_{0,si}$ is the initial radius of the Si particles. Then, the inelastic strain tensor, ϵ_{inel} , is also evaluated as:

$$\epsilon_{inel,m} = \left(\frac{V_m}{V_{0,m}} \right)^{\frac{1}{3}} - 1$$

Additional assumptions for the coupled electrochemical-mechanical model correspond to the fact that the contact interface between the electrode and the current collector is fixed. Also, we note that the mechanical analysis of this work mainly focuses on the electrode mesostructure changes. This is to say, even if we applied the mechanical properties of Si to a homogenized Si porous phase, the calculated stresses and strains cannot be directly related to the interactions between the Si particles. Thus, we only focus on the effects of the expansion of the Si phase on the displacements of the rest of electrode components. Additionally, interface between CBD and graphite (or Si) is also fixed. Therefore, no explicit detachment of CBD will occur as a result of active material volume expansion, even though high stress regions will be created.

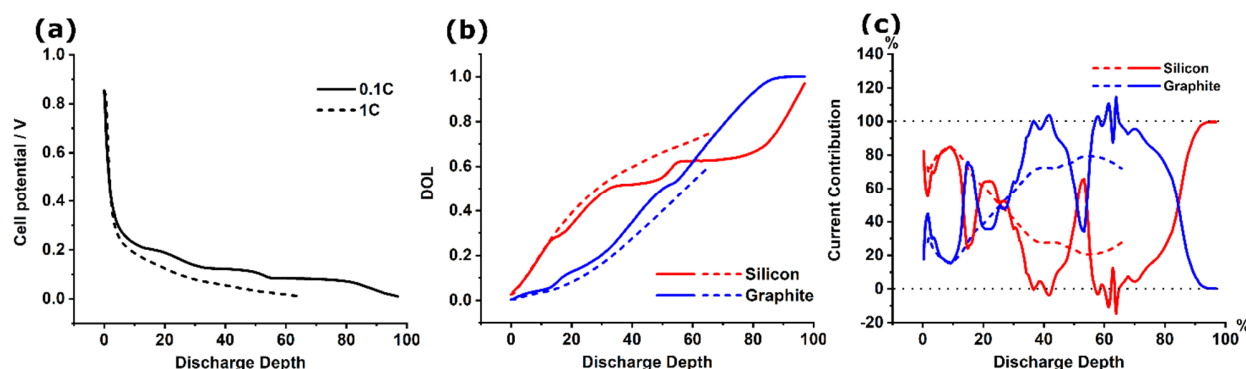


Figure 2: Cell potential (a) and degree of lithiation (b) and current contribution (c) curves, as function of the percentage of the discharge depth. Solid (dashed) lines represent discharge conditions at C rates of 0.1C (1C), with separated contributions for graphite (blue) and Si (red).

3. Results and discussions

We studied the discharge of a half cell model (Figure 1) at C rates 0.1C and 1C, with a cut-off potential of 0.01 V. The discharge curves of the graphite/Si composite electrode are shown in Figure 2(a). At 0.1C, the shape of the potential curves follow the known three plateaus of the graphite OCV. However, at 1C, these plateaus disappear, along the apparent capacity loss. Under 0.1C, the discharge depth reached 96.96%, while for 1C, only 65.64% of the capacity is used. This phenomenon is attributable to the overpotentials arising from mass transfer and interface reaction limitations, as well as internal electronic resistances. Nevertheless, when compared to a traditional single AM electrode, assessing the origin of the overpotentials becomes much more intricate when considering composite electrodes with more AM phases. This is because the differences in the electrochemical properties of both phases results in an interplay between both graphite and Si, making them experience different chemical environments.

3.1. Interfacial kinetics

Figure 2(b) shows the degree of lithiation (DOL) of graphite and Si, the system presents different behaviors under 0.1C and 1C. The situation at 1C is pretty straightforward, where the discharge process can be divided in two separated stages. First, the Si phase dominates the reaction, where the DOL quickly increases at the beginning of discharge. Then, graphite starts to dominate, where the slope of the Si DOL curve starts to decrease. This two-stage process can be further verified as shown in Figure 2(c), where the current contributions of each AM to the total current intersect in the middle of the discharge, therefore showing how each phase reacts at different discharge depths. There are several aspects that affect this behavior. Figure S6 (a,c) shows the average overpotentials calculated for graphite and Si, throughout the discharge process. We notice that the average value of the Si overpotential is maintained at very low values between -1.5 mV and -0.3 mV. On the contrary, graphite experiences a much larger overpotential ranging between -60 mV to -20 mV. In principle, this leads to much lower local current densities for the Si phase, when compared to graphite (Figure S6 (b,d)). However, due to the fact that the Si particles are considered as nanosized (45 nm), given their extremely high surface area ($\sim 90000 \mu\text{m}^2$), the Si phase actually accommodates rather large reaction currents. On the other side, graphite particles are much larger, and therefore their surface area is much lower (around $8400 \mu\text{m}^2$), thus resulting in overall lower total currents, where graphite dominates. In these regards, we note that this effects would attenuate by increasing the effective size of the Si particles. Indeed, the bigger the particles, the lower the surface area that would be available to

accommodate the current. Therefore, we could expect a shift in the DOL curves where graphite would start accommodating more current faster. Looking at this process in more detail, we see that at around 25% of discharge depth, the current contribution curves intersect, and graphite starts dominating the reactions at the second stage. At this transition point, the DOL of Si and graphite is of around 0.5 and 0.1, respectively, which relates to the first plateau in the graphite OCV curve. Afterwards, the graphite OCV drops below 0.2 V and thus starts further reacting and increasing its DOL. Additionally, we can differentiate how each phase experiences the faradaic current, by calculating their respective C rates (Figure S7). In fact, we can see that Si is experiencing C rates as high as 2.08 at 9% discharge depth. While the highest value for graphite reaches 1.33 at 54% discharge depth. Same for the 0.1C scenario, the materials are also experiencing different C rates. This deviation from the C rate that is applied to the composite electrode as a whole, evinces the difficulties when working with electrodes where multiple AM phases coexist, and demonstrates the need of additional considerations to make in the design of efficient composite anodes.

The situation gets more complicated when considering smaller C rates. Comparing to the two-stage process that we discussed at 1C, we can see that at 0.1C the DOL curves intersect at around 60% of discharge depth (Figure 2(b)). At this point, the relative concentration of lithium within graphite becomes larger than that of Si. We can see that their intersection points coincide with those of their respective OCV curves, where each slope changes corresponding to a phase transition of graphite. Therefore, the potential curve of the composite electrode somewhat resembles the shape of the graphite OCV. Looking at the evolution of the current contributions, we can see in Figure 2(c) that the behavior of the electrode is considerably more irregular at 0.1C. In general, the profile still follows the two-stage trend as 1C because of the relative

position of the OCV curves while taking surface area effects into account. However, we note that there are two particularly sharp fluctuations at 15% and 53% discharge depth. This can be understood by inspecting the average overpotential shown in Figure S6 (a,c), where the two peaks of

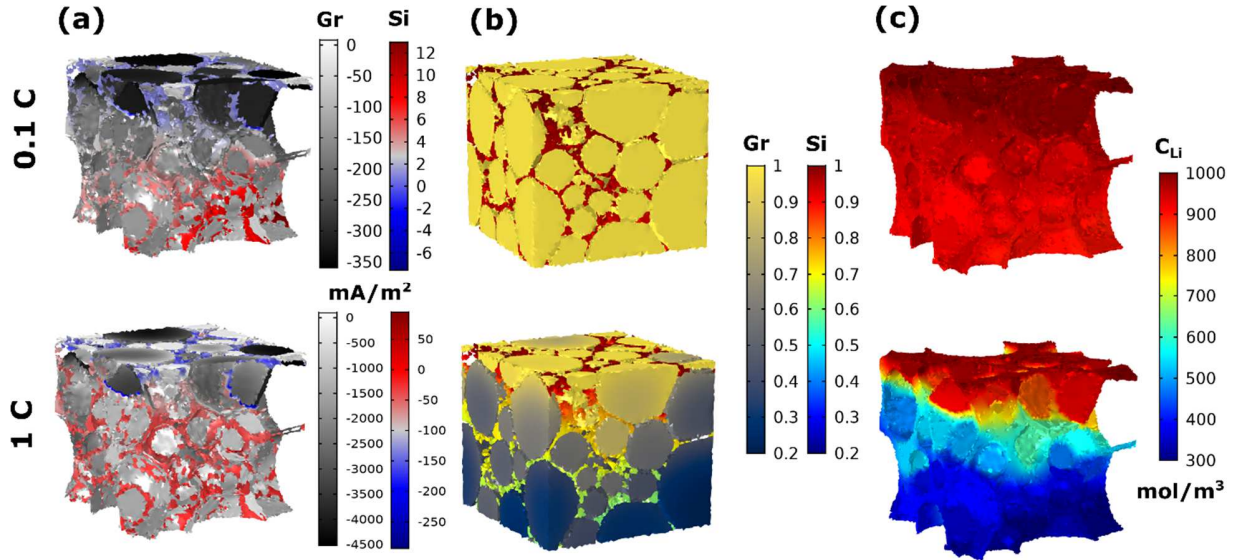


Figure 3: 3D maps of the local faradic current densities (a), DOL (b), and electrolyte lithium concentration (c). At 0.1C (top row) and 1C (bottom row) applied currents. The colorbars for each case are selected to ensure contrast between the graphite and Si phases.

overpotential at 15% and 53% discharge depth correspond to the abrupt change of current contribution profile.

Summing up, the DOL of a single AM electrode is expected to change monotonically during constant current operation, and this is not the case with our graphite/Si composite electrode. Additionally, as we can see from Figure 2(c), the current contribution from graphite exceeds 100% at around 60% discharge depth, while for Si it drops below 0%. This implies that some extra lithium exchange is happening between graphite and Si phases. Even if at 1C this effect is not visible through global averages such as the one of Figure 2(c), it still happens locally as can

be seen in Figure 3(a), where negative (positive) values represent lithiation (delithiation) zones. Of course, this same effect is also visible in the case of 0.1C. This lithium crosstalk between graphite and Si phases is recognized as an additional degradation mechanisms for the composite electrodes, and has recently been observed experimentally [60]. Which further strengthens the validity of our reported model. It's also worth to be noted that, for the 0.1C case, the crosstalk is happening at the point where silicon and graphite OCVs intersect. From this point, silicon OCV continues to drop below graphite, causing its overpotential become positive as shown in Figure S6 (a,c). Therefore, silicon is delithiating at this stage.

3.2. Mass transport

Another contributor to the electrode overpotential is the mass transfer limitation within the liquid phase. Figure 3(a) shows the heterogeneous local current densities throughout the electrode, where differences between graphite and Si phases are apparent again. The heterogeneity of the DOL is also clearly visible from Figure 3(b), where for both materials, the particles on the separator side (top) always show a higher DOL. At the end of the discharge, the differences between the DOL of graphite and Si is of 0.81 and 0.37, respectively. Thus, we can clearly say that the overpotential also arises from the lithium concentration gradient in the liquid phase, which is shown in Figure 3(c). Indeed, the concentration difference can be as high as 700 mol/m^3 , which largely affects the lithium exchange current density as included in the Butler-Volmer equation, causing low reaction current densities in low lithium concentration zones. Note that mass transport limitations should not, in principle, be an issue for such thin electrodes ($30 \mu\text{m}$) at 1C operation. However, we note that the model structure used in this work has a rather low porosity ($\sim 20\%$) which substantially hinders the effective diffusion of ions in the electrolyte. Additionally, a big part of this porosity is filled with the homogeneous Si domain, where lithium

ion transport is further slowed down. On the contrary, when using lower applied currents, the DOL distribution appears to be more homogeneous along the thickness of the model electrode, where a fully lithiated state is reached for both materials.

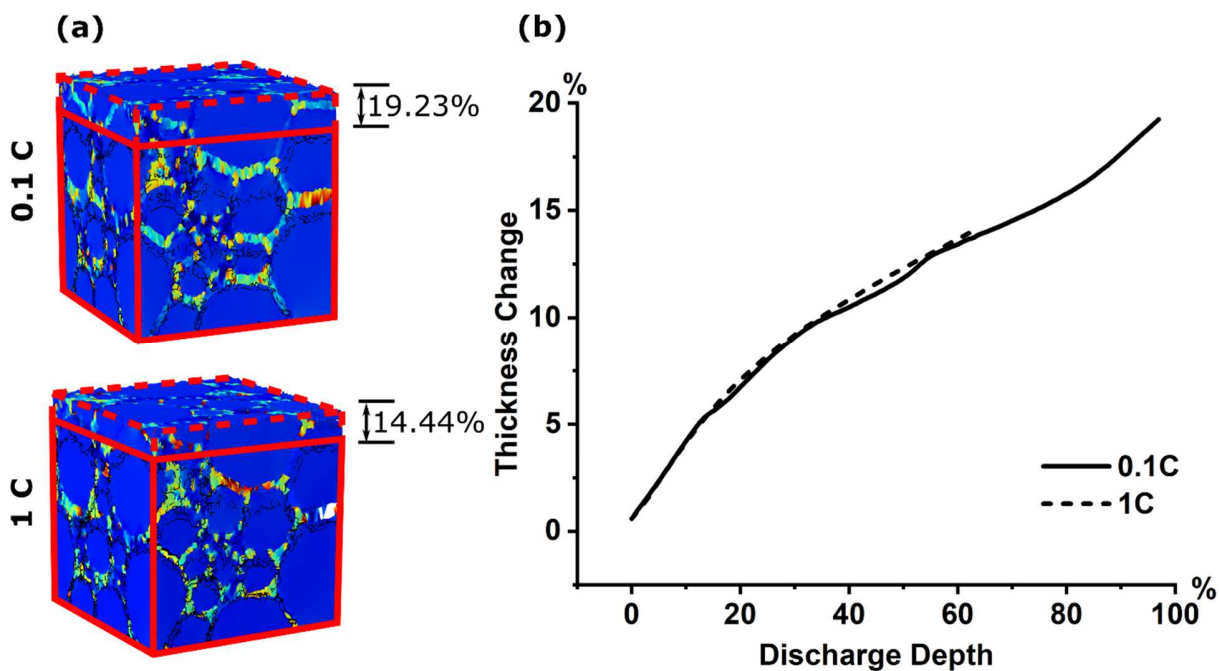


Figure 4: Structures of the discharged graphite/Si composite electrodes (after discharge) (a), and evolution of the electrode thickness as a function of the depth of discharge (b), for different applied currents 0.1C and 1C. The solid red box represents the dimensions of the pristine electrode, the dashed lines represent the degree of expansion after discharge.

3.3. Mechanics

As already mentioned, during discharge, both graphite and Si will swell when lithiated, which results in an overall expansion of the electrode (Figure 4(a)). The swelling of the active material components upon lithiation results in an electrode thickness expansion of 19.23% at 0.1C operation. Meanwhile, at 1C, given that the electrode did not reach its maximum capacity, it only expanded 14.44%. According to Gómez-Cámer *et. al.* [14] given an AM ratio of 4.75% Si + 90.25% graphite, with CMC/PAA as a binder material, the electrode expands 8.5% in one

discharge. Pietsch *et. al.* [61] reported electrode thickness change data in a discharge with a

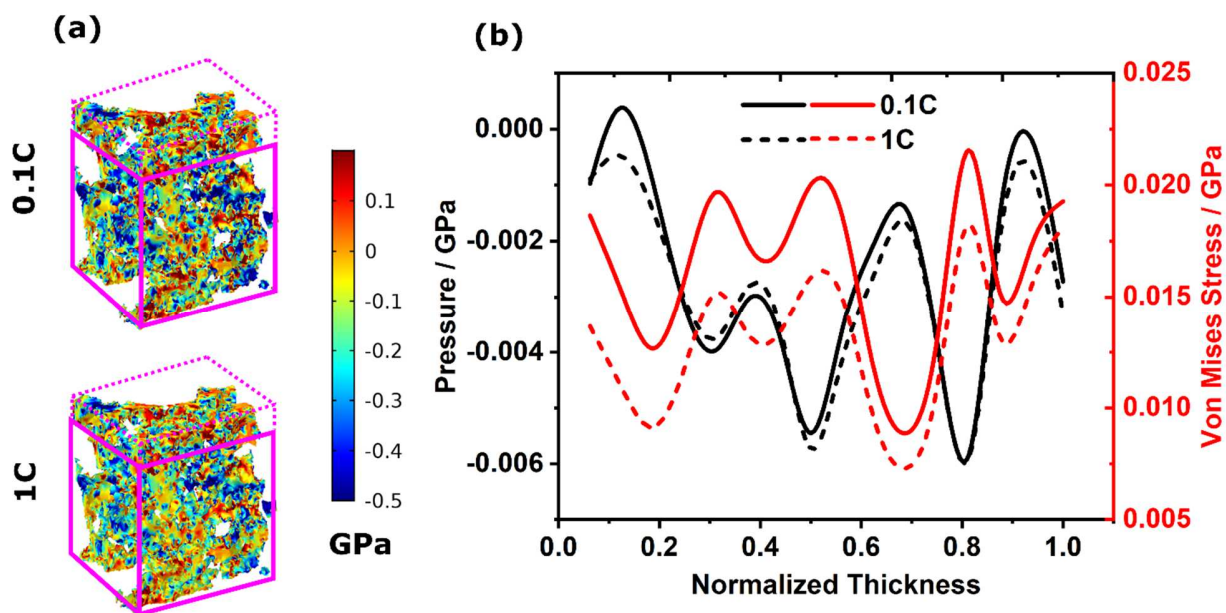


Figure 5: Pressure felt by the CBD phase (in GPa) at the end of discharge due to the volume expansion of the composite electrode AM components (a). Variation of the averaged pressure (black) and Von Mises stress (red) of slices along the electrode thickness. Results at 0.1C and 1C are shown in solid and dashed lines, respectively.

graphite/Si anode with 20 wt.% of Si. The cell showed around 30% to 40% expansion at the first cycle. Moreover, recently Moon *et. al.* [60] also reported electrode thickness variations during battery cycling, by considering a 15 wt.% of Si, and also showed an expansion of around 30% to 40%. Considering the 10 wt.% Si content of our model, and no additional degradation mechanisms, such as SEI formation or binder detachment, we think that our results are within a reasonable range. Figure 4(b) shows the evolution of the electrode thickness upon discharge, as we can see, the thickness of the electrodes increases faster when the Si is dominating the reaction. Additionally, small variations exist between 1C and 0.1C, where the latter results in slightly bigger thickness changes, given the higher DOL of the Si phase. Furthermore, we also found the expansion degree of the AM to be inhomogeneous. Figure S8 shows that the volumes ratios of the solid phases at the end of discharge vary across the electrode thickness. It is evident

that, at 1C, due to the DOL distribution caused by mass transfer limitations, leads to solid volume ratios that are larger near the separator side. Meanwhile, at 0.1C, the same volume ratios are maintained at both ends of the electrode. It is noteworthy that at both, 0.1C and 1C operation, the volume ratios in the middle of the electrode are always higher. This can be explained by a heterogeneous distribution of the graphite and Si content across the electrode thickness, as shown in Figure S9. Indeed, the higher Si content in the middle of the electrode results in a more severe expansion in this region. Apart from the structural changes of the graphite/Si composite electrodes upon discharge, the study of the internal stresses and strains between its constituent phases is essential to better understand their electrochemical performance. Specifically, binder failure is one of the main degradation factors of the graphite/Si composite electrodes, as explained earlier. This failure mechanisms often happen due to excessive strains and stresses that the binder cannot accommodate. With the present mesostructurally resolved model we can further assess the mechanical performance of the CBD domain. Figure 5(a) shows the pressure that is felt by the CBD domain due to the expansion of the AM phases. Negative pressures represent spatial regions where the CBD is being stretched, while positive pressures show the compression of the region in question. As illustrated, the CBD phase shows intertwined compressive and stretching pressures, where these conflicting interactions may result in different degradation mechanisms. In one hand, stretching regions may result in binder detachment from AM particles due to cohesion failure, which leads to a degradation of the structural integrity of the electrode, and a loss of electrical conductivity due to a damaged conductive percolation network. In order to give a closer look at this effects, we also analyzed the averaged pressure and Von Mises stress profiles along the thickness of the electrode. As can be seen in Figure 5(b) there is a clear correlation between the pressure felt by the CBD and its Von Mises stress, which

is an indicator of mechanical failure of the CBD phase. Along the whole electrode thickness the CBD feels a negative pressure where, due to the expansion of the graphite and Si phases, and the electrode thickness change, it is being elongated. This stretching effect is particularly strong in the middle of the electrode, as can also be visually seen from the higher concentration negative pressure (blue) regions in Figure 5(a). Interestingly, we see that the minima of the pressure profiles coincide with the maximum points of Von Mises stress, where again the maximum points of potential CBD failure are located in the middle of the electrode. Additionally, the Von Mises stress also shows particularly high values near the CC and Separator sides, even if pressure does not, indicating more potential degradation effects on these interfaces.

4. Conclusions

In this work, we have presented the first steps towards a 3D modelling approach to capture manufacturing-performance relationships of graphite/Si composite electrodes. We presented a workflow for the generation of the graphite/Si electrodes using Coarse-Grained Molecular Dynamics (CGMD), where the location of the Si particles was resolved by an *ad hoc* decoration approach, followed by a relaxation run. Then, these mesostructures were used as inputs for simulating the electrochemical performance of the graphite/Si composite electrodes by coupling electrochemistry and mechanics, given that Si suffers a ~300% volume expansion upon lithiation. The presented model captures fundamental phenomena regarding the complex interplay between the active material components in graphite/Si composite electrodes that have been experimentally observed. For instance, the model captures different stages of discharge, where graphite and Si contribute in varying percentages to the total electrode current, with a dependence on the applied C rate. Particularly, it is shown that Si dominates the first stages of the discharge process, where its degree of lithiation (DOL) increases sharply, while graphite

takes over at higher depths of discharge. Moreover, lithium crosstalk between graphite and Si phases was observed, where, due to differences in the electrode potentials of each materials, Si suffers local delithiation. Additionally, mass transport limitations were analyzed, where lithium concentration gradients in the electrolyte lead to a heterogeneous DOL of the active materials. Regarding the mechanics of the composite electrode, we show that the model captures some of the basic observables for mesostructural evolution upon Si and graphite volume expansion, such as the evolution of the electrode thickness. We also assessed the effects of stress and pressure on the electrode's CBD phase. The model captures potential failure points for the CBD phase, by looking at regions where Von Mises stresses are high. This high stress zones are correlated with negative pressure zones, indicating the stretching of the CBD phase. We argue that this potential failure points may cause detachment of the CBD phase from the active material particles, thus damaging the conductive percolation network. We also observe potential failure points at the CBD and CC (Separator) interfaces.

Summing up, all the aforementioned points have been a subject of discussion in many experimental works in the literature. We believe and we hope that the present model will help obtaining a more precise, and spatially resolved, understanding on the complex interplay between the electrochemical and mechanical behavior of composite graphite/Si anodes, eventually guiding the design of optimal electrode mesostructures, and potentially unlocking the next generation of lithium ion batteries.

Contributions:

C.L., O.A. Conceptualization, Methodology, Software, Validation, Investigation, Formal Analysis, Visualization; H.O. Investigation, Resources; T.L. Conceptualization, Methodology, Software; O.A. Writing – Original Draft; C.L., O.A., H.O., T.L., A.A.F. Writing – Review & Editing; A.A.F. Conceptualization, Supervision, Project Administration, Funding Acquisition.

Acknowledgements:

A.A.F., C.L., T.L. and H.O. acknowledge the European Union’s Horizon 2020 research and innovation programme for the funding support through the European Research Council (grant agreement 772873, “ARTISTIC” project). A.A.F. acknowledges ALISTORE European Research Institute for partial funding support. A.A.F. and O.A. acknowledges funding from the European Union’s Horizon 2020 research and innovation program under grant agreement No. 957189 (BIG-MAP). BATTERY 2030+ initiative under grant agreement No. 957213 is also acknowledged. A.A.F. acknowledges Institut Universitaire de France for the support. All authors acknowledge the TGCC Joliot-Curie (CEA) supercomputer for the computational support.

Funding:

The European Research Council (grant agreement 772873, “ARTISTIC” project). The European Union’s Horizon 2020 research and innovation program under grant agreement No. 957189 (BIG-MAP).

Declaration of competing interest

The authors declare that they have no known competing financial interests or personal relationships that could have influenced the work reported in this paper

References

- [1] A. Opitz, P. Badami, L. Shen, K. Vignarooban, A.M. Kannan, Can Li-Ion batteries be the panacea for automotive applications?, *Renew. Sustain. Energy Rev.* 68 (2017) 685–692. <https://doi.org/https://doi.org/10.1016/j.rser.2016.10.019>.
- [2] Y.-K. Sun, Promising All-Solid-State Batteries for Future Electric Vehicles, *ACS Energy Lett.* 5 (2020) 3221–3223. <https://doi.org/10.1021/acseenergylett.0c01977>.
- [3] J. Janek, W.G. Zeier, A solid future for battery development, *Nat. Energy.* 1 (2016) 16141. <http://dx.doi.org/10.1038/nenergy.2016.141>.
- [4] J.F. DeCarolis, D.W. Keith, The economics of large-scale wind power in a carbon constrained world, *Energy Policy.* 34 (2006) 395–410. <https://doi.org/https://doi.org/10.1016/j.enpol.2004.06.007>.
- [5] H.S. Laine, J. Salpakari, E.E. Looney, H. Savin, I.M. Peters, T. Buonassisi, Meeting global cooling demand with photovoltaics during the 21st century, *Energy Environ. Sci.* (2019). <https://doi.org/10.1039/C9EE00002J>.
- [6] Y. Li, Y. Lu, P. Adelhelm, M.M. Titirici, Y.S. Hu, Intercalation chemistry of graphite: Alkali metal ions and beyond, *Chem. Soc. Rev.* 48 (2019) 4655–4687. <https://doi.org/10.1039/c9cs00162j>.
- [7] M.N. Obrovac, V.L. Chevrier, Alloy Negative Electrodes for Li-Ion Batteries, (2014). <https://doi.org/10.1021/cr500207g>.
- [8] X. Zuo, J. Zhu, P. Müller-Buschbaum, Y.J. Cheng, Silicon based lithium-ion battery anodes: A chronicle perspective review, *Nano Energy.* 31 (2017) 113–143. <https://doi.org/10.1016/j.nanoen.2016.11.013>.
- [9] S. Chae, M. Ko, K. Kim, K. Ahn, J. Cho, Confronting Issues of the Practical Implementation of Si Anode in High-Energy Lithium-Ion Batteries, *Joule.* 1 (2017) 47–60. <https://doi.org/10.1016/j.joule.2017.07.006>.
- [10] X. Su, Q. Wu, J. Li, X. Xiao, A. Lott, W. Lu, B.W. Sheldon, J. Wu, Silicon-Based Nanomaterials for Lithium-Ion Batteries: A Review, *Adv. Energy Mater.* 4 (2014) 1300882. <https://doi.org/https://doi.org/10.1002/aenm.201300882>.
- [11] Y. Yang, W. Yuan, W. Kang, Y. Ye, Y. Yuan, Z. Qiu, C. Wang, X. Zhang, Y. Ke, Y. Tang, Silicon-nanoparticle-based composites for advanced lithium-ion battery anodes, *Nanoscale.* 12 (2020) 7461–7484. <https://doi.org/10.1039/c9nr10652a>.
- [12] P. Li, H. Kim, S.T. Myung, Y.K. Sun, Diverting Exploration of Silicon Anode into

- Practical Way: A Review Focused on Silicon-Graphite Composite for Lithium Ion Batteries, *Energy Storage Mater.* 35 (2021) 550–576. <https://doi.org/10.1016/j.ensm.2020.11.028>.
- [13] C.-H. Yim, S. Niketic, N. Salem, O. Naboka, Y. Abu-Lebdeh, Towards Improving the Practical Energy Density of Li-Ion Batteries: Optimization and Evaluation of Silicon:Graphite Composites in Full Cells, *J. Electrochem. Soc.* 164 (2017) A6294–A6302. <https://doi.org/10.1149/2.0481701jes>.
- [14] J.L. Gómez-Cámer, C. Bünzli, M.M. Hantel, T. Poux, P. Novák, On the correlation between electrode expansion and cycling stability of graphite/Si electrodes for Li-ion batteries, *Carbon N. Y.* 105 (2016) 42–51. <https://doi.org/https://doi.org/10.1016/j.carbon.2016.04.022>.
- [15] X. Zhao, S. Niketic, C. Yim, J. Zhou, J. Wang, Y. Abu-lebdeh, Revealing the Role of Poly (vinylidene fluoride) Binder in Si / Graphite Composite Anode for Li-Ion Batteries, 3 (2018) 11684–11690. <https://doi.org/10.1021/acsomega.8b01388>.
- [16] S. Müller, P. Pietsch, B.E. Brandt, P. Baade, V. De Andrade, F. De Carlo, V. Wood, Quantification and modeling of mechanical degradation in lithium-ion batteries based on nanoscale imaging, *Nat. Commun.* 9 (2018) 1–8. <https://doi.org/10.1038/s41467-018-04477-1>.
- [17] M. Wetjen, D. Pritzl, R. Jung, S. Solchenbach, R. Ghadimi, H.A. Gasteiger, Differentiating the Degradation Phenomena in Silicon-Graphite Electrodes for Lithium-Ion Batteries, *J. Electrochem. Soc.* 164 (2017) A2840–A2852. <https://doi.org/10.1149/2.1921712jes>.
- [18] F. Jeschull, Y. Surace, S. Zürcher, G. Lari, M.E. Spahr, P. Novák, S. Trabesinger, Graphite Particle-Size Induced Morphological and Performance Changes of Graphite–Silicon Electrodes, *J. Electrochem. Soc.* 167 (2020) 100535. <https://doi.org/10.1149/1945-7111/ab9b9a>.
- [19] O.O. Taiwo, M. Loveridge, S.D. Beattie, D.P. Finegan, R. Bhagat, D.J.L. Brett, P.R. Shearing, Investigation of cycling-induced microstructural degradation in silicon-based electrodes in lithium-ion batteries using X-ray nanotomography, *Electrochim. Acta.* 253 (2017) 85–92. <https://doi.org/10.1016/j.electacta.2017.08.161>.
- [20] C. Stetson, Z. Huey, A. Downard, Z. Li, B. To, A. Zakutayev, C.S. Jiang, M.M. Al-Jassim, D.P. Finegan, S.D. Han, S.C. Decaluwe, Three-Dimensional Mapping of Resistivity and Microstructure of Composite Electrodes for Lithium-Ion Batteries, *Nano Lett.* 20 (2020) 8081–8088. <https://doi.org/10.1021/acs.nanolett.0c03074>.
- [21] M. Ebner, F. Geldmacher, F. Marone, M. Stampanoni, V. Wood, X-Ray Tomography of Porous, Transition Metal Oxide Based Lithium Ion Battery Electrodes, *Adv. Energy Mater.* 3 (2013) 845–850. <https://doi.org/https://doi.org/10.1002/aenm.201200932>.
- [22] P. Pietsch, V. Wood, X-Ray Tomography for Lithium Ion Battery Research: A Practical Guide, *Annu. Rev. Mater. Res.* 47 (2017) 451–479. <https://doi.org/10.1146/annurev->

matsci-070616-123957.

- [23] A.A. Franco, A. Rucci, D. Brandell, C. Frayret, M. Gaberscek, P. Jankowski, P. Johansson, Boosting Rechargeable Batteries R&D by Multiscale Modeling: Myth or Reality?, *Chem. Rev.* 119 (2019) 4569–4627. <https://doi.org/10.1021/acs.chemrev.8b00239>.
- [24] M. Chouchane, E.N. Primo, A.A. Franco, Mesoscale Effects in the Extraction of the Solid-State Lithium Diffusion Coefficient Values of Battery Active Materials: Physical Insights from 3D Modeling, *J. Phys. Chem. Lett.* 11 (2020) 2775–2780. <https://doi.org/10.1021/acs.jpcllett.0c00517>.
- [25] A.C. Ngandjong, T. Lombardo, E.N. Primo, M. Chouchane, A. Shodiev, O. Arcelus, A.A. Franco, Investigating electrode calendaring and its impact on electrochemical performance by means of a new discrete element method model: Towards a digital twin of Li-Ion battery manufacturing, *J. Power Sources.* 485 (2021) 229320. <https://doi.org/https://doi.org/10.1016/j.jpowsour.2020.229320>.
- [26] M. Chouchane, A. Rucci, T. Lombardo, A. Ngandjong C., A.A. Franco, Lithium ion battery electrodes predicted from manufacturing simulations: Assessing the impact of the carbon-binder spatial location on the electrochemical performance, *J. Power Sources.* 444 (2019) 227285. <https://doi.org/https://doi.org/10.1016/j.jpowsour.2019.227285>.
- [27] A. Shodiev, E.N. Primo, M. Chouchane, T. Lombardo, A.C. Ngandjong, A. Rucci, A.A. Franco, 4D-resolved physical model for Electrochemical Impedance Spectroscopy of Li(Ni_{1-x-y}Mn_xCo_y)O₂-based cathodes in symmetric cells: Consequences in tortuosity calculations, *J. Power Sources.* 454 (2020) 227871. <https://doi.org/10.1016/j.jpowsour.2020.227871>.
- [28] A. Shodiev, E. Primo, O. Arcelus, M. Chouchane, M. Osenberg, A. Hilger, I. Manke, J. Li, A.A. Franco, Insight on electrolyte infiltration of lithium ion battery electrodes by means of a new three-dimensional-resolved lattice Boltzmann model, *Energy Storage Mater.* 38 (2021) 80–92. <https://doi.org/https://doi.org/10.1016/j.ensm.2021.02.029>.
- [29] I. Srivastava, D.S. Bolintineanu, J.B. Lechman, S.A. Roberts, Controlling Binder Adhesion to Impact Electrode Mesostuctures and Transport, *ACS Appl. Mater. Interfaces.* 12 (2020) 34919–34930. <https://doi.org/10.1021/acsami.0c08251>.
- [30] D. Westhoff, I. Manke, V. Schmidt, Generation of virtual lithium-ion battery electrode microstructures based on spatial stochastic modeling, *Comput. Mater. Sci.* 151 (2018) 53–64. <https://doi.org/https://doi.org/10.1016/j.commatsci.2018.04.060>.
- [31] J. Joos, A. Buchele, A. Schmidt, A. Weber, E. Ivers-Tiffée, Virtual Electrode Design for Lithium-Ion Battery Cathodes, *Energy Technol.* 2000891 (2021). <https://doi.org/10.1002/ente.202000891>.
- [32] A.C. Ngandjong, A. Rucci, M. Maiza, G. Shukla, J. Vazquez-Arenas, A.A. Franco, Multiscale Simulation Platform Linking Lithium Ion Battery Electrode Fabrication Process with Performance at the Cell Level, *J. Phys. Chem. Lett.* 8 (2017) 5966–5972.

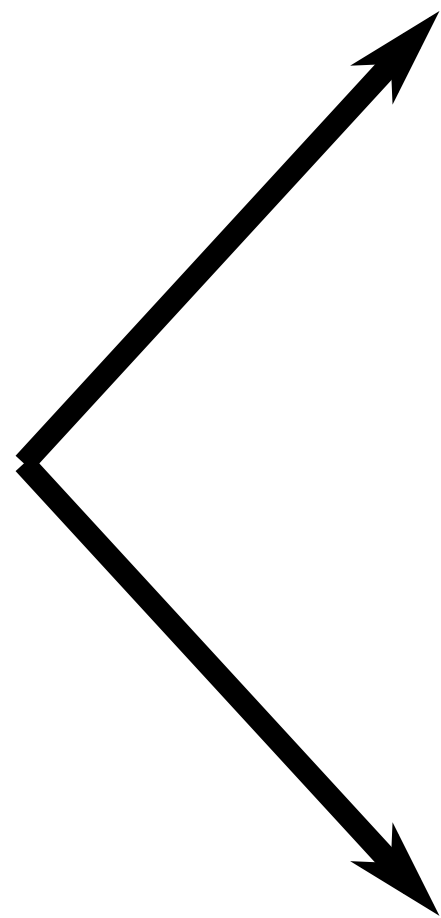
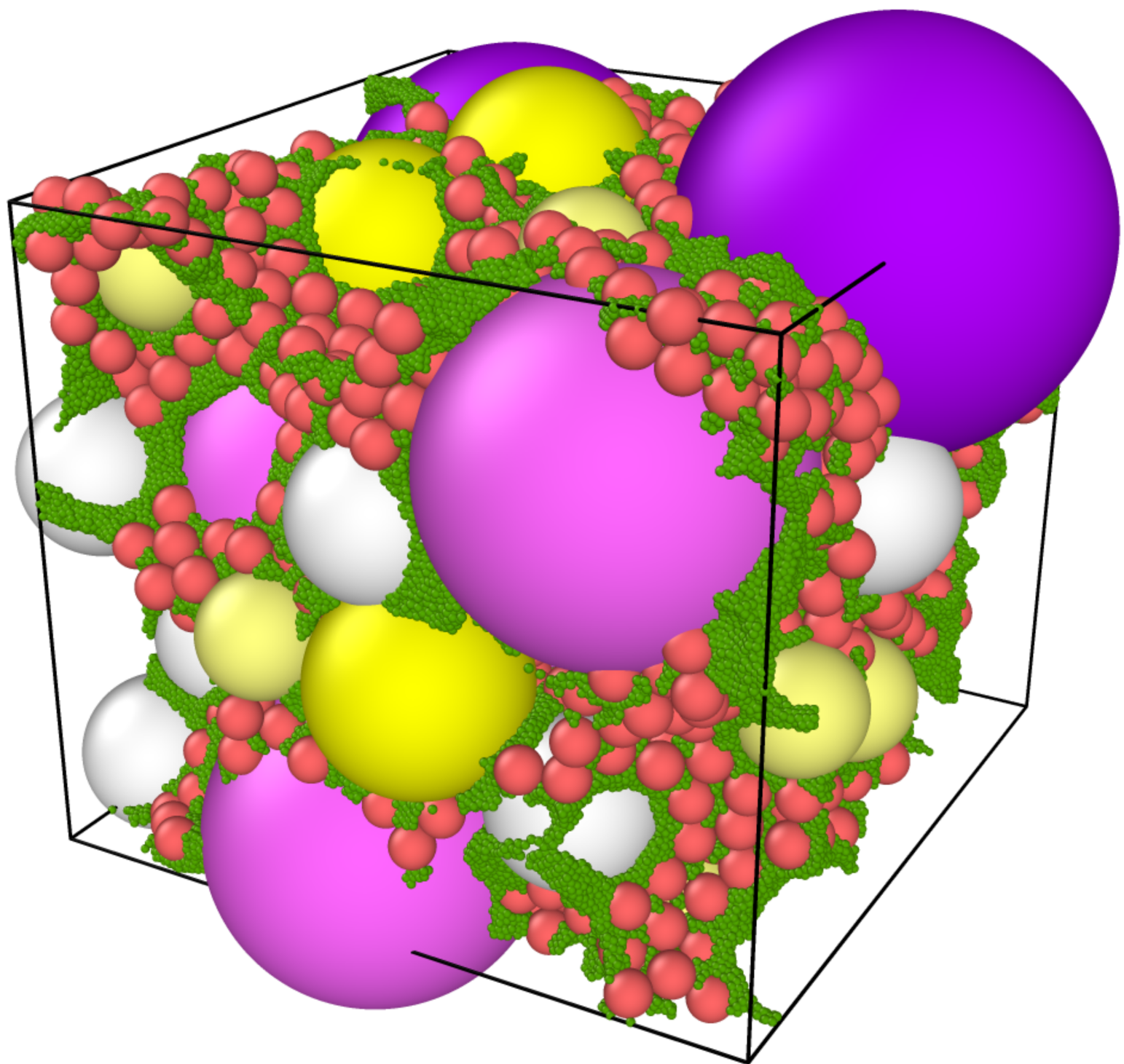
<https://doi.org/10.1021/acs.jpcllett.7b02647>.

- [33] M.M. Forouzan, C. Chao, D. Bustamante, B.A. Mazzeo, D.R. Wheeler, Experiment and simulation of the fabrication process of lithium-ion battery cathodes for determining microstructure and mechanical properties, *J. Power Sources*. 312 (2016) 172–183. <https://doi.org/10.1016/j.jpowsour.2016.02.014>.
- [34] C. Sangrós Giménez, C. Schilde, L. Froböse, S. Ivanov, A. Kwade, Mechanical, Electrical, and Ionic Behavior of Lithium-Ion Battery Electrodes via Discrete Element Method Simulations, *Energy Technol.* 8 (2020) 1900180. <https://doi.org/https://doi.org/10.1002/ente.201900180>.
- [35] C. Sangrós Giménez, B. Finke, C. Nowak, C. Schilde, A. Kwade, Structural and mechanical characterization of lithium-ion battery electrodes via DEM simulations, *Adv. Powder Technol.* 29 (2018) 2312–2321. <https://doi.org/https://doi.org/10.1016/j.appt.2018.05.014>.
- [36] C. Sangrós Giménez, B. Finke, C. Schilde, L. Froböse, A. Kwade, Numerical simulation of the behavior of lithium-ion battery electrodes during the calendaring process via the discrete element method, *Powder Technol.* 349 (2019) 1–11. <https://doi.org/https://doi.org/10.1016/j.powtec.2019.03.020>.
- [37] A. Gayon-Lombardo, L. Mosser, N.P. Brandon, S.J. Cooper, Pores for thought: generative adversarial networks for stochastic reconstruction of 3D multi-phase electrode microstructures with periodic boundaries, *Npj Comput. Mater.* 6 (2020) 82. <https://doi.org/10.1038/s41524-020-0340-7>.
- [38] S. Kench, S.J. Cooper, Generating three-dimensional structures from a two-dimensional slice with generative adversarial network-based dimensionality expansion, *Nat. Mach. Intell.* 3 (2021) 299–305. <https://doi.org/10.1038/s42256-021-00322-1>.
- [39] M. Chouchane, O. Arcelus, A.A. Franco, Heterogeneous Solid-Electrolyte Interphase in Graphite Electrodes Assessed by 4D-Resolved Computational Simulations, *Batter. Supercaps.* n/a (2021). <https://doi.org/https://doi.org/10.1002/batt.202100030>.
- [40] C.-F. Sun, K. Karki, Z. Jia, H. Liao, Y. Zhang, T. Li, Y. Qi, J. Cumings, G.W. Rubloff, Y. Wang, A Beaded-String Silicon Anode, *ACS Nano.* 7 (2013) 2717–2724. <https://doi.org/10.1021/nn4001512>.
- [41] M. Wang, X. Xiao, Investigation of the chemo-mechanical coupling in lithiation/delithiation of amorphous Si through simulations of Si thin films and Si nanospheres, *J. Power Sources.* 326 (2016) 365–376. <https://doi.org/https://doi.org/10.1016/j.jpowsour.2016.07.011>.
- [42] F. Hao, X. Gao, D. Fang, Diffusion-induced stresses of electrode nanomaterials in lithium-ion battery: The effects of surface stress, *J. Appl. Phys.* 112 (2012) 103507. <https://doi.org/10.1063/1.4767913>.
- [43] M. Wang, X. Xiao, X. Huang, A multiphysics microstructure-resolved model for silicon

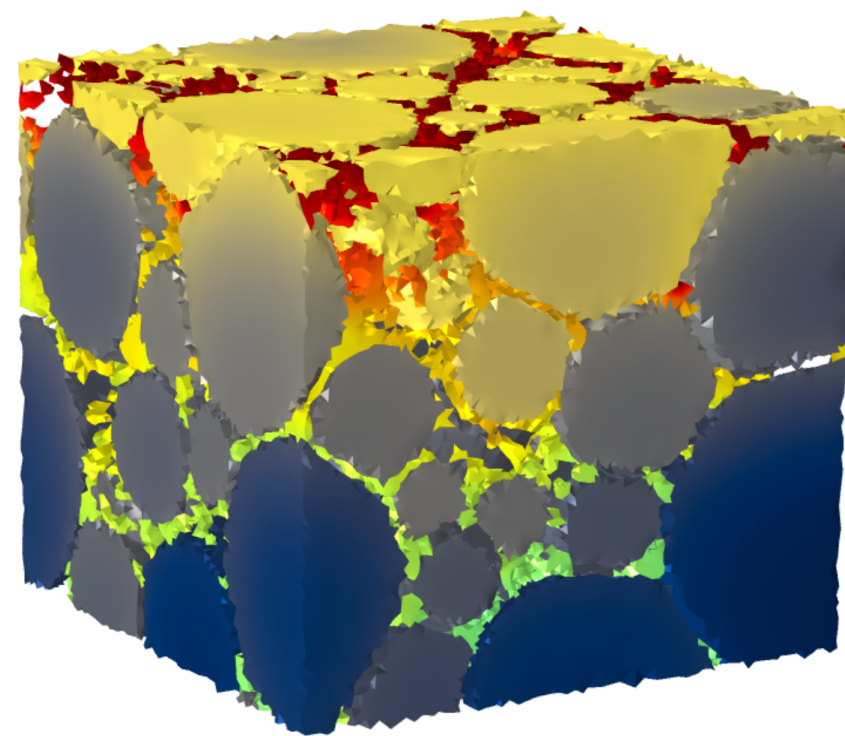
- anode lithium-ion batteries, *J. Power Sources*. 348 (2017) 66–79. <https://doi.org/https://doi.org/10.1016/j.jpowsour.2017.02.037>.
- [44] X.H. Liu, L. Zhong, S. Huang, S.X. Mao, T. Zhu, J.Y. Huang, Size-Dependent Fracture of Silicon Nanoparticles During Lithiation, *ACS Nano*. 6 (2012) 1522–1531. <https://doi.org/10.1021/nn204476h>.
- [45] H. Yang, F. Fan, W. Liang, X. Guo, T. Zhu, S. Zhang, A chemo-mechanical model of lithiation in silicon, *J. Mech. Phys. Solids*. 70 (2014) 349–361. <https://doi.org/https://doi.org/10.1016/j.jmps.2014.06.004>.
- [46] J. Sturm, A. Rheinfeld, I. Zilberman, F.B. Spingler, S. Kosch, F. Frie, A. Jossen, Modeling and simulation of inhomogeneities in a 18650 nickel-rich, silicon-graphite lithium-ion cell during fast charging, *J. Power Sources*. 412 (2019) 204–223. <https://doi.org/https://doi.org/10.1016/j.jpowsour.2018.11.043>.
- [47] V. Vanpeene, P. Soucy, J. Xiong, N. Dupré, B. Lestriez, L. Roué, Sequential focused ion beam scanning electron microscopy analyses for monitoring cycled-induced morphological evolution in battery composite electrodes. Silicon-graphite electrode as exemplary case, *J. Power Sources*. 498 (2021) 229904. <https://doi.org/https://doi.org/10.1016/j.jpowsour.2021.229904>.
- [48] A.J. Louli, J. Li, S. Trussler, C.R. Fell, J.R. Dahn, Volume, Pressure and Thickness Evolution of Li-Ion Pouch Cells with Silicon-Composite Negative Electrodes, *J. Electrochem. Soc.* 164 (2017) A2689–A2696. <https://doi.org/10.1149/2.1691712jes>.
- [49] A. Kraysberg, Y. Ein-Eli, Conveying Advanced Li-ion Battery Materials into Practice The Impact of Electrode Slurry Preparation Skills, *Adv. Energy Mater.* 6 (2016) 1600655. <https://doi.org/10.1002/aenm.201600655>.
- [50] V. Wenzel, H. Nirschl, D. Nötzel, Challenges in Lithium-Ion-Battery Slurry Preparation and Potential of Modifying Electrode Structures by Different Mixing Processes, *Energy Technol.* 3 (2015) 692–698. <https://doi.org/10.1002/ente.201402218>.
- [51] W. Bauer, D. Nötzel, Rheological properties and stability of NMP based cathode slurries for lithium ion batteries, *Ceram. Int.* 40 (2014) 4591–4598. <https://doi.org/10.1016/j.ceramint.2013.08.137>.
- [52] H. Bockholt, W. Haselrieder, A. Kwade, Intensive powder mixing for dry dispersing of carbon black and its relevance for lithium-ion battery cathodes, *Powder Technol.* 297 (2016) 266–274. <https://doi.org/10.1016/j.powtec.2016.04.011>.
- [53] L. Zielke, T. Hutzenlaub, D.R. Wheeler, C.-W. Chao, I. Manke, A. Hilger, N. Paust, R. Zengerle, S. Thiele, Three-Phase Multiscale Modeling of a LiCoO₂ Cathode: Combining the Advantages of FIB–SEM Imaging and X-Ray Tomography, *Adv. Energy Mater.* 5 (2015) 1401612. <https://doi.org/https://doi.org/10.1002/aenm.201401612>.
- [54] H. Li, X. Huang, L. Chen, G. Zhou, Z. Zhang, D. Yu, Y. Jun Mo, N. Pei, Crystal structural evolution of nano-Si anode caused by lithium insertion and extraction at room

- temperature, *Solid State Ionics*. 135 (2000) 181–191. [https://doi.org/10.1016/S0167-2738\(00\)00362-3](https://doi.org/10.1016/S0167-2738(00)00362-3).
- [55] R. Andersson, G. Hernández, K. Edström, J. Mindemark, Micro versus Nano: Impact of Particle Size on the Flow Characteristics of Silicon Anode Slurries, *Energy Technol.* 8 (2020) 1–7. <https://doi.org/10.1002/ente.202000056>.
- [56] <https://lammmps.sandia.gov>.
- [57] T. Lombardo, J. Hoock, E. Primo, C. Ngandjong, M. Duquesnoy, A.A. Franco, Accelerated Optimization Methods for Force-Field Parametrization in Battery Electrode Manufacturing Modeling, *Batter. Supercaps.* 3 (2020) 721-730. <https://doi.org/10.1002/batt.202000049>.
- [58] A.P. Tran, S. Yan, Q. Fang, Improving model-based functional near-infrared spectroscopy analysis using mesh-based anatomical and light-transport models, *Neurophotonics*. 7 (2020) 1. <https://doi.org/10.1117/1.nph.7.1.015008>.
- [59] M.N. Obrovac, L. Christensen, D.B. Le, J.R. Dahn, Alloy Design for Lithium-Ion Battery Anodes, *J. Electrochem. Soc.* 154 (2007) A849. <https://doi.org/10.1149/1.2752985>.
- [60] J. Moon, H.C. Lee, H. Jung, S. Wakita, S. Cho, J. Yoon, J. Lee, A. Ueda, B. Choi, S. Lee, K. Ito, Y. Kubo, A.C. Lim, J.G. Seo, J. Yoo, S. Lee, Y. Ham, W. Baek, Y.G. Ryu, I.T. Han, Interplay between electrochemical reactions and mechanical responses in silicon–graphite anodes and its impact on degradation, *Nat. Commun.* 12 (2021). <https://doi.org/10.1038/s41467-021-22662-7>.
- [61] P. Pietsch, D. Westhoff, J. Feinauer, J. Eller, F. Marone, M. Stampanoni, V. Schmidt, V. Wood, Quantifying microstructural dynamics and electrochemical activity of graphite and silicon-graphite lithium ion battery anodes, *Nat. Commun.* 7 (2016) 1–11. <https://doi.org/10.1038/ncomms12909>.

Graphite/Silicon electrode model



Electrochemistry



Mechanics

